Angewandte Chemie
Eine Zeitschrift der Gesellschaft Deutscher Chemiker

Supporting Information

# Electronic Structure and Magnetic Anisotropy of an Unsaturated Cyclopentadienyl Iron(I) Complex with 15 Valence Electrons

*Uttam Chakraborty, Serhiy Demeshko, Franc Meyer,* Christophe Rebreyend, Bas de Bruin,* Mihail Atanasov,* Frank Neese,* Bernd Mühldorf, and Robert Wolf**

ange_201702454_sm_miscellaneous_information.pdf

**Table of Contents**

## 1. Experimental Section

### 1.1 General Considerations

All experiments were performed under an atmosphere of dry argon, by using standard Schlenk and glovebox techniques. Solvents were purified, dried, and degassed with an MBraun SPS800 solvent purification system. NMR spectra were recorded on BrukerAvance 300 and Avance 400 spectrometers at 300 K and internally referenced to residual solvent resonances. The $^{1}$H NMR signals of complexes **2** and **3** were assigned by $^{1}$H,$^{1}$H COSY experiments and the relative integration of the signals. Melting points were measured in sealed capillaries on a Stuart SMP10 melting point apparatus. UV-vis spectra were recorded on a Varian Cary 50 spectrometer. Elemental analyses were determined by the analytical department of Regensburg University. Complex **1**[1] and IMe$_2$*i*Pr$_2$[2] were prepared according to the literature procedures. *N*,*N*-dimethylamine borane was purchased from *Sigma-Aldrich* and sublimed before use.

### 1.2 Synthesis of [Cp$^{Ar}$Fe(IMe$_2$*i*Pr$_2$)] (1)

A mixture of [Cp$^{Ar}$Fe($\mu$-Br)]$_2$ (**3**) (200 mg, 0.14 mmol) and IMe$_2$*i*Pr$_2$ (50 mg, 0.28 mmol) was dissolved in 10 mL of benzene. The deep orange solution was stirred for one hour and treated with $KC_8$ (40 mg, 0.30 mmol). The mixture slowly turned to a dark yellow suspension upon stirring for two days. The $^{1}$H NMR spectrum of an aliquot showed the formation of **2** as the sole product. The suspension was filtered, and the dark yellow filtrate was evaporated to dryness and powderized. Complex **3** was obtained as a very air sensitive, brownish yellow solid. Yield: 183 mg (0.22 mmol, 78%). M.p. >210 °C (decomp.); UV-vis (toluene): $\lambda_{max}$/nm ($\varepsilon_{max}$ / L·mol$^{-1}$·cm$^{-1}$) = 341 (19596). $^{1}$H NMR (400.13 MHz, $C_6D_6$, 300 K): −36.1 (s br, 10H, 5 × *o*/*m*-C*H*, Cp$^{Ar}$), −3.7 (s br, 15H, 5 × C*H*$_3$, Cp$^{Ar}$), 0.6 (s br, 12H, 2 × CH(C*H*$_3$)$_2$, IMe$_2$*i*Pr$_2$), 8.9 (s br, 10H, 5 × C*H*$_2$, Cp$^{Ar}$), 11.9 (s br, 10H, 5 × *o*/*m*-C*H*, Cp$^{Ar}$), 60.8 (s br, 6H, backbone C*H*$_3$, IMe$_2$*i*Pr$_2$); the resonance of the methine proton of the *iso*-propyl group was not observed presumably due to severe broadening of this signal. $\mu_{eff}$ ($C_6D_6$): 5.4(1) $\mu_B$. Elemental analysis calcd. for $C_{56}H_{65}N_2Fe$ (Mw = 822.00 g/mol): C 81.83, H 7.97, N 3.41; found: C 81.52, H 7.92, N 3.13.

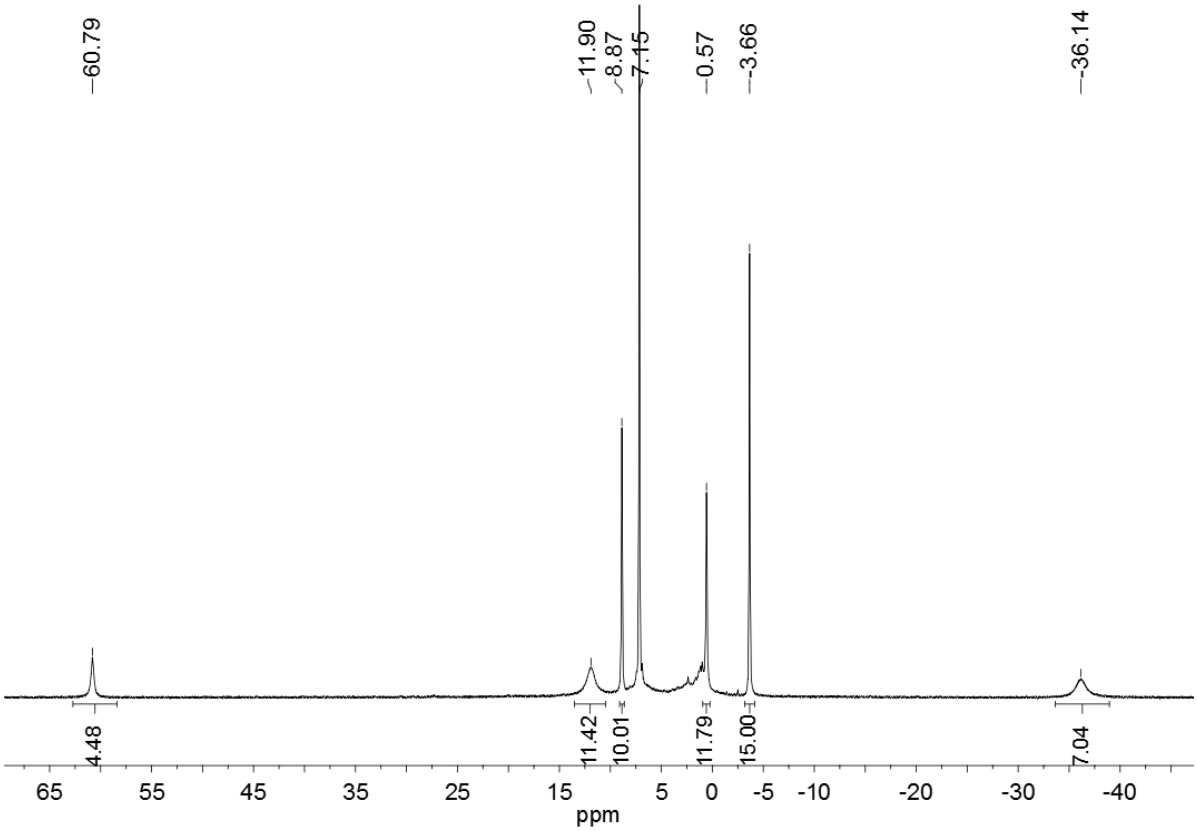


**Figure S1**. $^{1}$H NMR spectrum (400.13 MHz) of **1** in $C_6D_6$ at 300.

### 1.3 Synthesis and Characterization of [Cp$^{Ar}$FeBr(IMe$_2$*i*Pr$_2$)] (2)

A mixture of [Cp$^{Ar}$Fe($\mu$-Br)]$_2$ (**1**) (231 mg, 0.16 mmol) and IMe$_2$*i*Pr$_2$ (58 mg, 0.32 mmol) was dissolved in 10 mL of benzene. The deep orange solution was stirred for one hour and evaporated completely to a deep orange sticky solid which was triturated with 10 mL of *n*-hexane. Complex **2** was obtained as a pale yellow powder after drying *in vacuo*. Yield: 220 mg (0.24 mmol, 76%). Yellow, crystalline **2** is air-sensitive, thermally stable and dissolves well in THF and benzene, but only sparingly in diethyl ether. M.p. >163 °C (decomp.); UV-vis (toluene): $\lambda_{max}$/nm ($\varepsilon_{max}$ / L·mol$^{-1}$·cm$^{-1}$) = 348 (17716). $^{1}$H NMR (400.13 MHz, $C_6D_6$, 300 K): −53.4 (s br, 2H, 2 × C*H*(CH$_3$)$_2$, IMe$_2$*i*Pr$_2$), −22.9 (s br, 10H, 5 × *o*/*m*-C*H*, Cp$^{Ar}$), −5.3 (s, 15H, 5 × C*H*$_3$, Cp$^{Ar}$), 3.8 (s br, 12H, 2 × CH(C*H*$_3$)$_2$, IMe$_2$*i*Pr$_2$), 10.7 (s, 10H, 5 × C*H*$_2$, Cp$^{Ar}$), 28.6 (s br, 10H, 5 × *o*/*m*-C*H*, Cp$^{Ar}$), 42.9 (s br, 6H, backbone C*H*$_3$, IMe$_2$*i*Pr$_2$). $\mu_{eff}$ ($C_6D_6$): 5.8(1) $\mu_B$. Elemental analysis calcd. for $C_{56}H_{65}N_2FeBr$ (Mw = 901.90 g/mol): C 74.58, H 7.26, N 3.11; found: C 75.05, H 7.26, N 2.74.

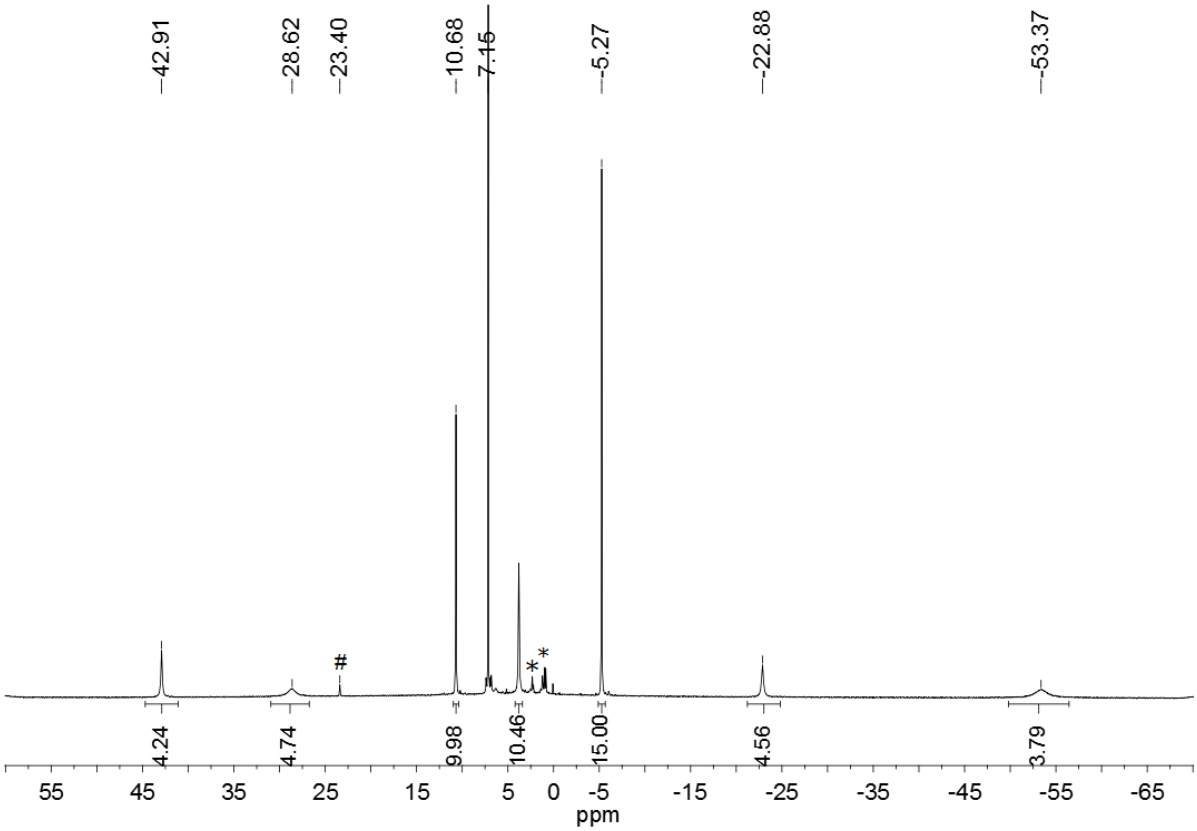


**Figure S2.** $^{1}$H NMR spectrum (400.13 MHz) of **2** in $C_6D_6$ at 300 K; * denotes ($C_5(C_6H_4$-4-Et$)_5H$) observed as an impurity; signals marked with # represent an impurity.

## 1.4 Dehydrogenation of *N,N*-dimethylamineborane (DMAB)

### 1.4.1 Dehydrogenation of DMAB using 1 (5 mol%)

For the $H_2$ evolution experiments, complex **1** (10 mg, 0.012 mmol) dissolved in 1 mL of toluene was treated with DMAB (13.6 mg, 0.23 mmol) dissolved in toluene (1 mL). The $H_2$ evolved in the reaction was collected in a burette set up and its volume determined.[3] The volume of $H_2$ was corrected for the water vapor pressure at 25 °C.[3]

For the NMR experiments, complex **1** (20 mg, 0.024 mmol) and DMAB (27 mg, 0.46 mmol) were mixed in a 25 mL glass-vial and treated with toluene (3 mL). The resulting yellow-brown solution was stirred in an open vial inside a glove box. An aliquot (0.1 mL) was taken out at each time interval and analyzed by $^{11}$B{$^{1}$H} NMR spectroscopy.

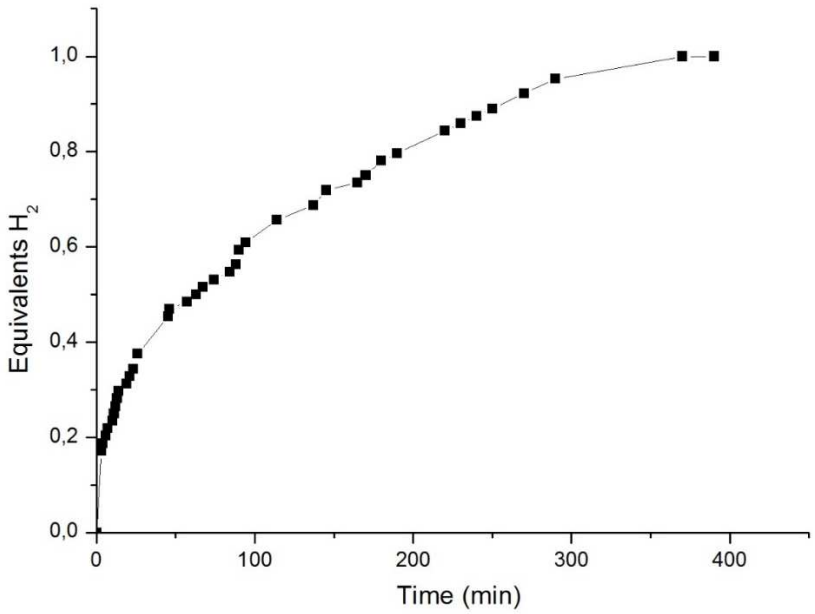


**Figure S3**. Dehydrogenation of DMAB in an open system in toluene at 298 K catalyzed by **1** (5 mol%).

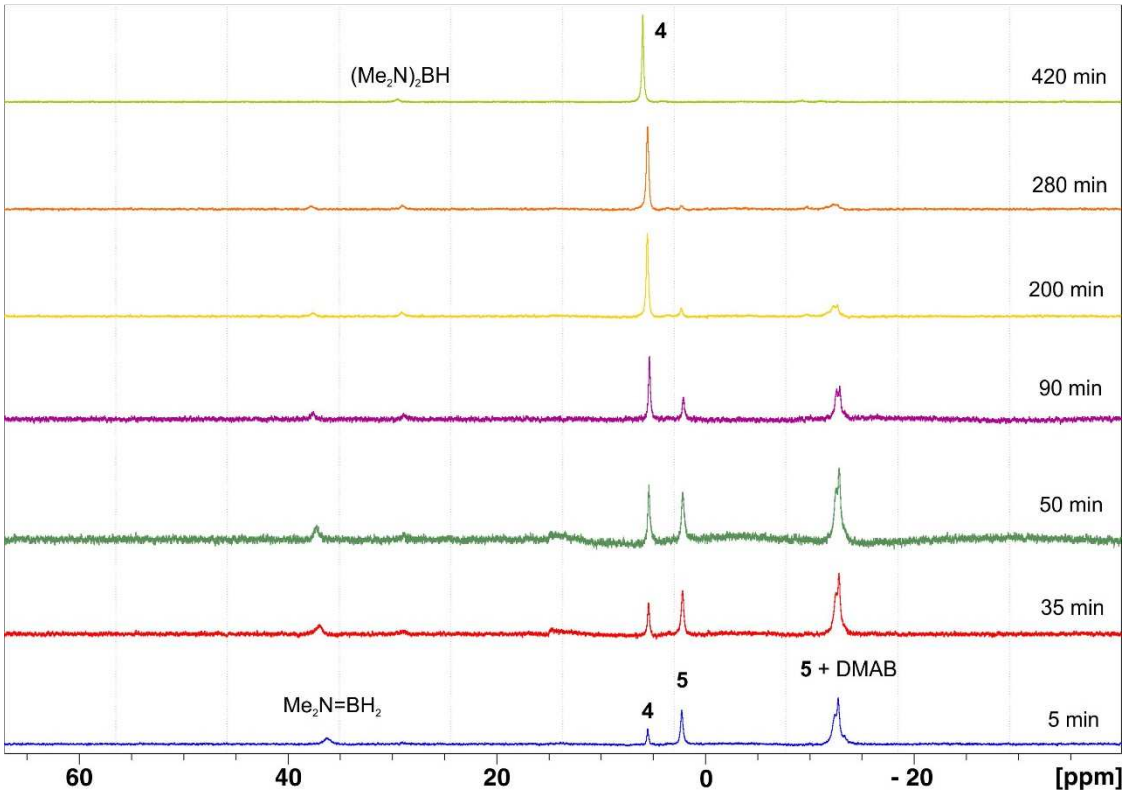


**Figure S4**. $^{11}B\{^1H\}$ NMR (128.38 MHz) monitoring of the catalytic dehydrogenation of DMAB with **1** (5 mol%) in toluene at 300 K. **4** = 1,3-diaza-2,4-diboretane; **6** = $Me_2HN\text{-}BH_2\text{-}NMe_2\text{-}BH_3$.

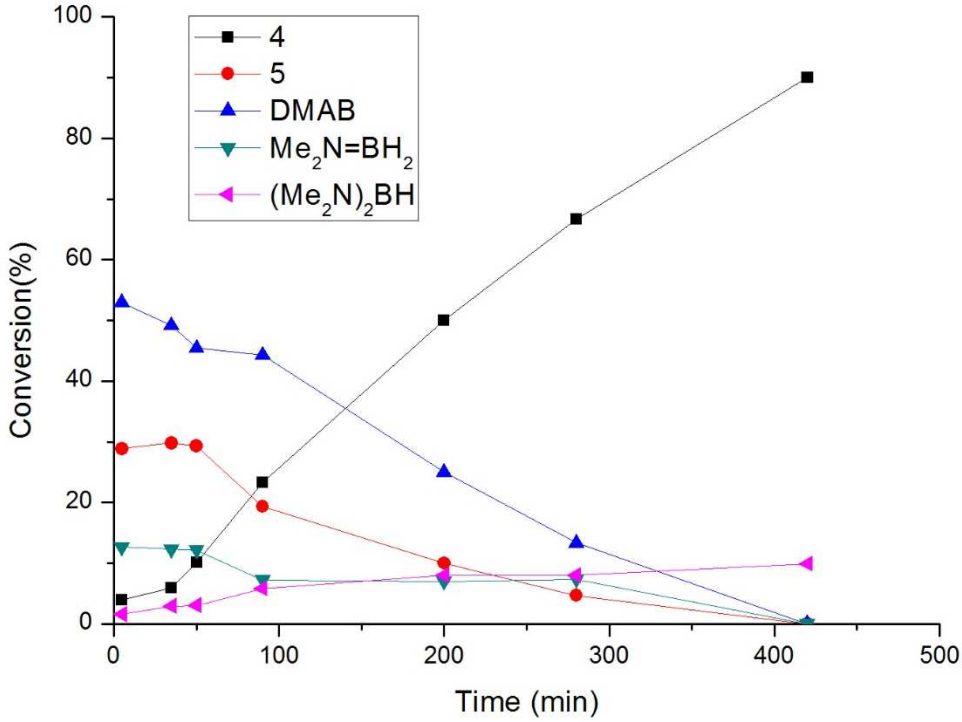


**Figure S5**. Conversion vs. time plot obtained by $^{11}B\{^{1}H\}$ NMR monitoring (Figure S4) of the catalytic dehydrogenation of DMAB with **1** (5 mol%) in toluene at 300 K; **4** = 1,3-diaza-2,4-diboretane; **6** = $Me_2HN\text{-}BH_2\text{-}NMe_2\text{-}BH_3$.

### 1.4.2 Poisoning experiments with $P(OMe)_3$ and dibenzo[a,e]cyclooctatetraene (DCT)

**Experimental details:** Complex **1** (10 mg, 0.012 mmol) dissolved in toluene (1 mL) was treated with DMAB (13.6 mg, 0.23 mmol) dissolved in toluene (1 mL). The $H_2$ evolved in the reaction was collected in a burette set up and its volume determined. The recorded volume of $H_2$ was corrected for the water vapor pressure at 25 °C.[3] For the poisoning with DCT, a solution of DCT (5 mg, 0.024 mmol in 0.5 mL toluene) was added after 15 minutes. For poisoning with $P(OMe)_3$, a stock solution of the poison (0.024 M in toluene) was added after 15 min. The following amounts of the stock solution were added in three separate catalytic runs: 1 mol% $P(OMe_3)$ (0.1 mL, 0.0024 mmol, 0.2 equiv. relative to **1**), 2.5 mol% $P(OMe)_3$ (0.25 mL, 0.006 mmol, 0.5 equiv. relative to **1**), and 5 mol% $P(OMe)_3$ (0.5 mL, 0.012 mmol relative to **1**).

**Interpretation of the poisoning studies:** The results of the poisoning studies with dibenzo[a,e]cyclooctatetraene (DCT) and $P(OMe_3)$ hint at a homogeneous mechanism. Addition of DCT (10 mol%) at 30% conversion resulted in the immediate and complete inhibition of the reaction (Figure S6). DCT selectively binds homogeneous metal species as a consequence of its rigid tub-like structure and π-acceptor ability.[4,5] The reaction was only

partially inhibited by substoichiometric amounts of $P(OMe)_3$ (1 mol%, 2.5 mol%, and 5 mol%, Figure S7). The rate decrease is proportional to the amount of $P(OMe)_3$ added (Figure S8). This is an indication for a homogeneous catalyst species. Further information was obtained by $^{11}B$ NMR spectroscopy. The diborazane $Me_2HN\text{-}BH_2\text{-}NMe_2\text{-}BH_3$ (**6**) was detected as the dominant intermediate observed along with traces of dimethylaminoborane $Me_2N{=}BH_2$ (Figure S4). The formation of **6** can be explained by a homogeneous on-metal dehydrogenation process occurring in solution.[6]

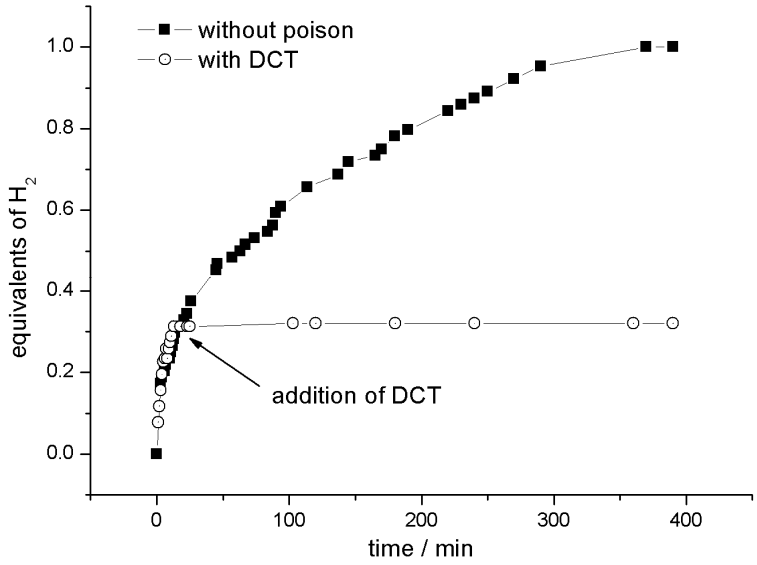


**Figure S6**. Dehydrogenation of DMAB in an open system in toluene at 298 K catalyzed by **1** (5 mol%). Addition of DCT (10 mol%, i.e. 2 equiv. relative to **1**) after 15 min results in the complete inhibition of catalysis, which may indicate a homogeneous reaction mechanism.

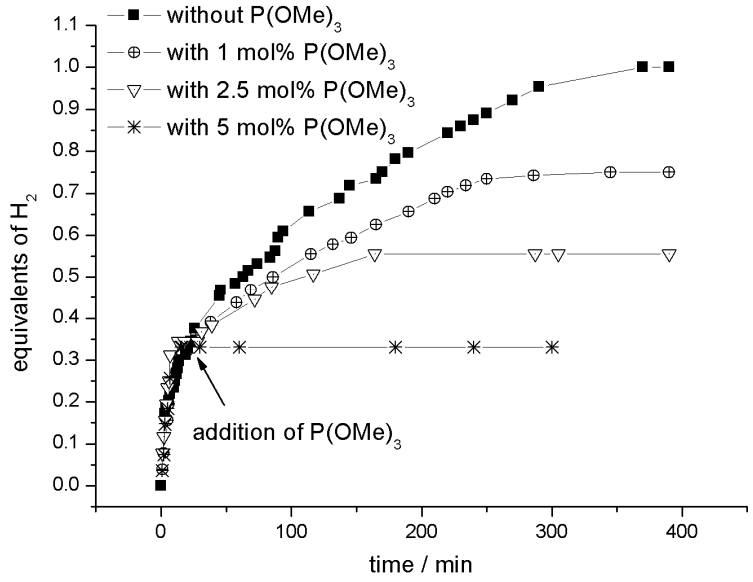


**Figure S7**. Dehydrogenation of DMAB in an open system in toluene at 298 K catalyzed by **1** (5 mol%) with addition of $P(OMe)_3$ (1, 2.5 and 5 mol%, i.e. 0.2, 0.5 and 1 equiv. relative to **1**) after 15 minutes.

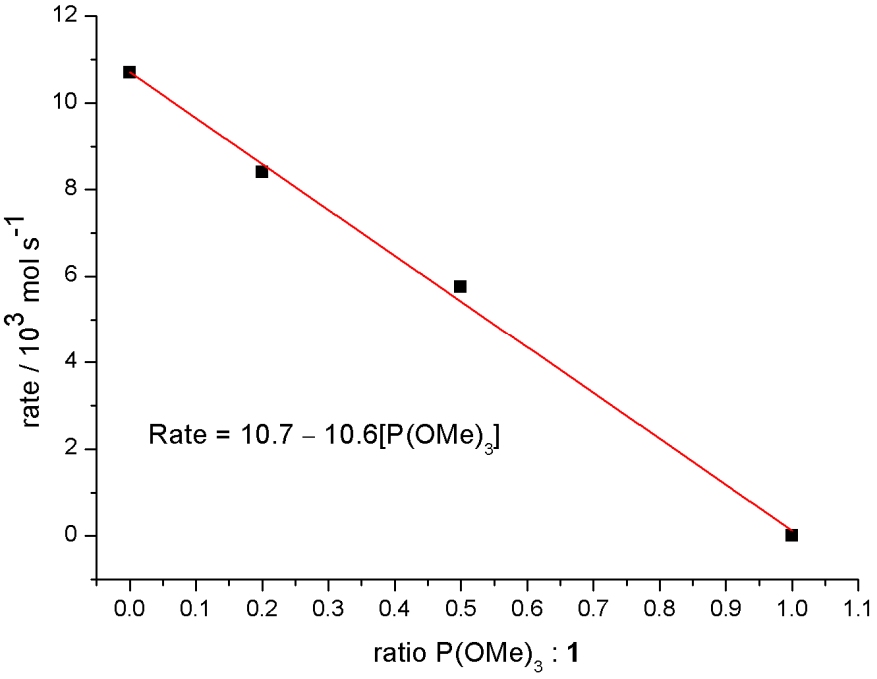


**Figure S8**. Plot of the initial rate of the reaction observed after adding the catalyst poison $P(OMe)_3$. The reaction rate drops proportionally to the amount of catalyst poison added.

### 1.4.3 Dehydrogenation of DMAB catalyzed by 1 (10 mol%); repeated addition of DMAB

For the NMR experiments, complex **1** (20 mg, 0.024 mmol) and DMAB (13 mg, 0.22 mmol) were mixed in a 25 mL glass-vial and treated with toluene (3 mL). The resulting yellow-brown solution was stirred in open vial inside a glove box. An aliquot (0.1 mL) was taken out after 30 min for NMR spectroscopy. The $^{11}B\{^1H\}$ NMR spectrum suggested that the conversion of DMAB to 1,3-diaza-2,4-diboretane (**4**) was almost complete. A second equivalent of DMAB (13 mg, 0.22 mmol) was added to the reaction vial, and the reaction progress was monitored by $^{11}B\{^1H\}$ NMR spectroscopy.

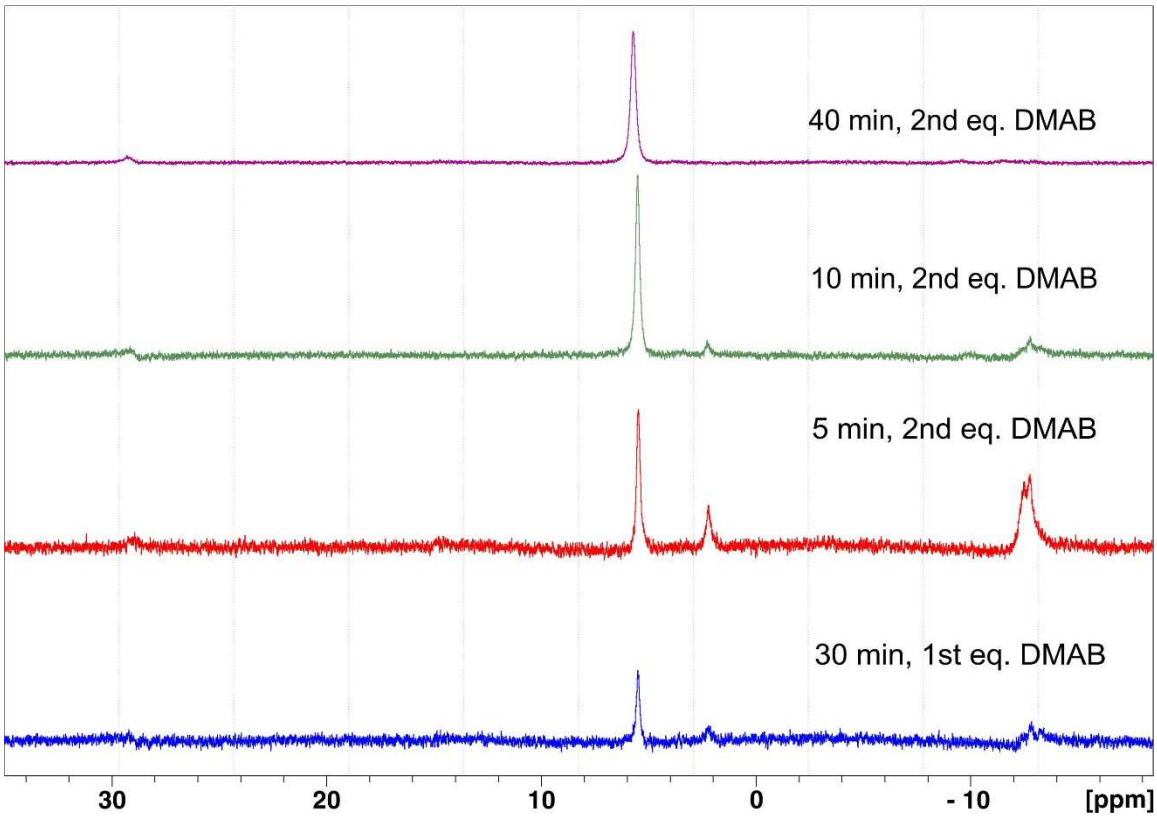


**Figure S9**. $^{11}B\{^{1}H\}$ NMR (128.38 MHz) monitoring of the catalytic dehydrogenation of DMAB with **1** (10 mol%) in toluene at 300 K; **4** = 1,3-diaza-2,4-diboretane; **6** = $Me_2HN\text{-}BH_2\text{-}NMe_2\text{-}BH_3$.

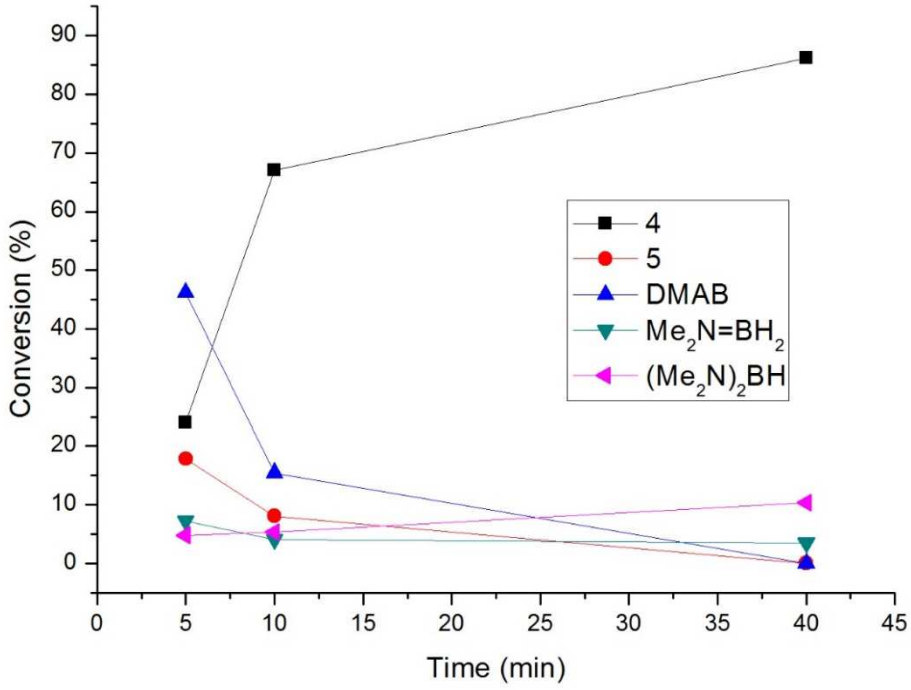


**Figure S10**. Conversion vs. time plot obtained by $^{11}B\{^{1}H\}$ NMR monitoring (Figure S9) of the catalytic dehydrogenation of DMAB with **1** (10 mol%) in toluene at 300 K after the addition of the second equivalent of DMAB; **4** = 1,3-diaza-2,4-diboretane; **6** = $Me_2HN\text{-}BH_2\text{-}NMe_2\text{-}BH_3$.

## 2 X-ray crystallography

Yellow X-ray quality crystals **1** formed from an *n*-hexane solution –35 °C. Orange-yellow crystals of **2** suitable for X-ray crystallography were obtained by slow evaporation of the benzene solution of **2**. The crystals were processed at an Agilent Technologies SuperNova diffractometer with microfocus Cu radiation. The CrysAlis software was used to apply Gaussian absorption corrections.[7] Using Olex2,[8] the structures were solved with direct methods by ShelXT and refined with ShelXL using least squares minimization.[9] of the structure determinations are given below. The crystallographic information files (CIF) have been deposited at the CCDC, 12 Union Road, Cambridge, CB21EZ, U.K., and can be obtained on request free of charge, by quoting the publication citation and deposition numbers CCDC 1511169 and 1511169.

**Crystal Data for 1:** $C_{112}H_{130}Fe_2N_4$ (*M* =1643.89 g/mol): monoclinic, space group $P2_1/n$ (no. 14), *a* = 27.7251(4) Å, *b* = 11.89744(14) Å, *c* = 27.9757(4) Å, *β* = 95.0066(12)°, *V* = 9192.8(2) Å$^3$, *Z* = 4, *T* = 123.0(1) K, μ(CuKα) = 2.909 mm$^{-1}$, *Dcalc* = 1.188 g/cm$^3$, 73263 reflections measured (8.08° ≤ 2Θ ≤ 148.34°), 18283 unique ($R_{int}$ = 0.0465, $R_{sigma}$ = 0.0366) which were used in all calculations. The final $R_1$ was 0.0487 (I > 2σ(I)) and $wR_2$ was 0.1355 (all data).

**Crystal Data for 2:** $C_{112}H_{130}Br_2Fe_2N_4$ (*M* =1803.80 g/mol): triclinic, space group P-1 (no. 2), *a* = 14.7157(5) Å, *b* = 16.7719(5) Å, *c* = 21.1773(7) Å, *α* = 88.842(3)°, *β* = 71.382(3)°, *γ* = 87.579(3)°, *V* = 4948.7(3) Å$^3$, *Z* = 2, *T* = 123.0(1) K, μ(Cu Kα) = 3.655 mm$^{-1}$, *Dcalc* = 1.2104 g/cm$^3$, 36611 reflections measured (6.84° ≤ 2Θ ≤ 148.36°), 19170 unique ($R_{int}$ = 0.0317, $R_{sigma}$ = 0.0414) which were used in all calculations. The final $R_1$ was 0.0629 (I>=2u(I)) and $wR_2$ was 0.1474 (all data).

The solid-state molecular structures of **2** is displayed in Figure S10. The Fe–Cp$^{Ar}$(centroid) distance (2.020(1) and 2.038(1) Å) in the two legged piano-stool complex **2** is consistent with a high-spin Fe(II) complex, such as dimeric starting material **3** (1.93856(8) Å), its THF adduct $[Cp^{Ar}Fe(\square\text{-}Br)(THF)]_2$ (2.042(1) Å) and the alkyl-substituted cyclopentadienyl analogue $[Cp^{tBu3}FeI(I\textit{i}Pr_2Me_2)]$ (2.0 Å) ($Cp^{tBu3}$ = η$^5$-1,2,4-$(Me_3C)_3C_5H_2$).[10] The Fe–$C_{carbene}$ bond length (2.110(3) and 2.128(3) Å) is in good agreement with that in $[Cp^{tBu3}FeI(I\textit{i}Pr_2Me_2)]$ (2.124(1) Å) and significantly longer than in [Cp*FeCl(NHC)] [NHC = 1,3-dimesitylimidazol-2-ylidene (IMes), 1,3-diisopropyl-4,5-dimethylimidazol-2-ylidene (IPr)], which might be a consequence

of steric repulsion of the *i*Pr substituents on the NHC and the aryl groups of the cyclopentadienyl moiety.[11]

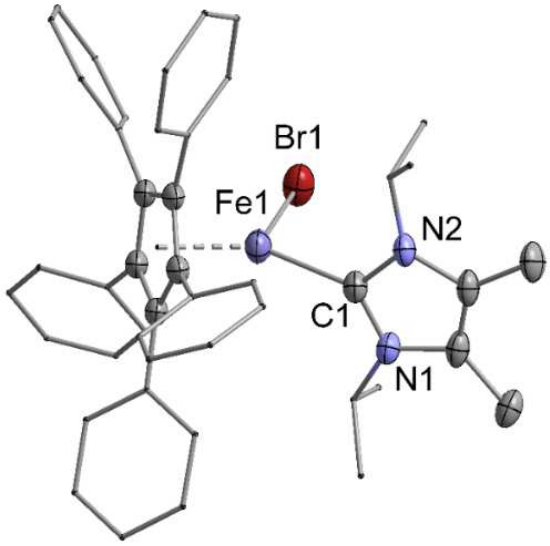


**Figure S11**. Solid-state molecular structure of **2**. Thermal ellipsoids are drawn at the 5% probability level. The H atoms and ethyl group on the aryl rings are omitted for clarity. Selected bond distances (Å) and bond angles (°) [bond lengths and bond angles for a second molecule in the asymmetric unit are given in the parentheses]: Fe1–C1 2.110(3) [2.128(3)], Fe1–$Cp^{Ar}$(centroid) 2.020(1) [2.038(1)]; $Cp^{Ar}$(centroid)–Fe1–C1 134.142(3) [134.780(3)], $Cp^{Ar}$(centroid)–Fe1–Br1 125.572(3) [127.561(4)], Fe1–C1–N1 125.5(2) [124.2(2)], Fe1–C1–N2 128.5(2) [130.2(2)].

## 3 Magnetic properties

Temperature-dependent magnetic susceptibility measurements were carried out with a *Quantum-Design* MPMS-XL-5 SQUID magnetometer equipped with a 5 Tesla magnet in the range from 2 to 210 K in a magnetic field of 0.5 T. The polycrystalline sample was contained in a gel bucket, covered with a drop of low viscosity perfluoropolyether based inert oil Fomblin Y45 to fix the crystals, and fixed in a non-magnetic sample holder. The maximum measuring temperature of 210 K was chosen because of the pour point of the oil, in order to keep the oil in the frozen state and to avoid therefore the orientation of the crystals in the magnetic field. Each raw data file for the measured magnetic moment was corrected for the diamagnetic contribution of the gel bucket and of the inert oil according to $M^{dia} = \chi_g \cdot m \cdot H$, with experimentally obtained gram susceptibility of gel bucket ($\chi_g = -5.70 \cdot 10^{-7}$ emu/(g·Oe) and of the oil ($\chi_g = -3.82 \cdot 10^{-7}$ emu/(g·Oe)). The molar susceptibility data were corrected for the diamagnetic contribution according to $\chi_M^{dia}$(sample) = $-0.5 \cdot M \cdot 10^{-6}$ cm$^3$·mol$^{-1}$.[12]

Experimental $\chi_M T$ vs. $T$ data as well as the VTVH magnetization measurements data were simultaneously modelled using a fitting procedure to the following spin Hamiltonian for one iron(I) $S = 3/2$ ion with Zeeman splitting and zero-field splitting:

$$\hat{H} = \mu_B(S_x g_x B_x + S_y g_y B_y + S_z g_z B_z) + D\left[\hat{S}_z^2 - \frac{1}{3}S(S+1) + E/D(\hat{S}_x^2 - \hat{S}_y^2)\right] \quad \text{(eq. 1)}$$

Full-matrix diagonalization of the spin Hamiltonian was performed with the *julX_2s* program (E. Bill, Max-Planck Institute for Chemical Energy Conversion, Mülheim/Ruhr, Germany, **2014**). Matrix diagonalization is done with the routine ZHEEV from the LAPACK numerical package. Parameter optimization is performed with the simplex routine AMOEBA from NUMERICAL RECIPES. The best fit values are $g_x = g_y = 2.18$, $g_z = 2.52$, $D = -33.4$ cm$^{-1}$ and $E/D = 0$.

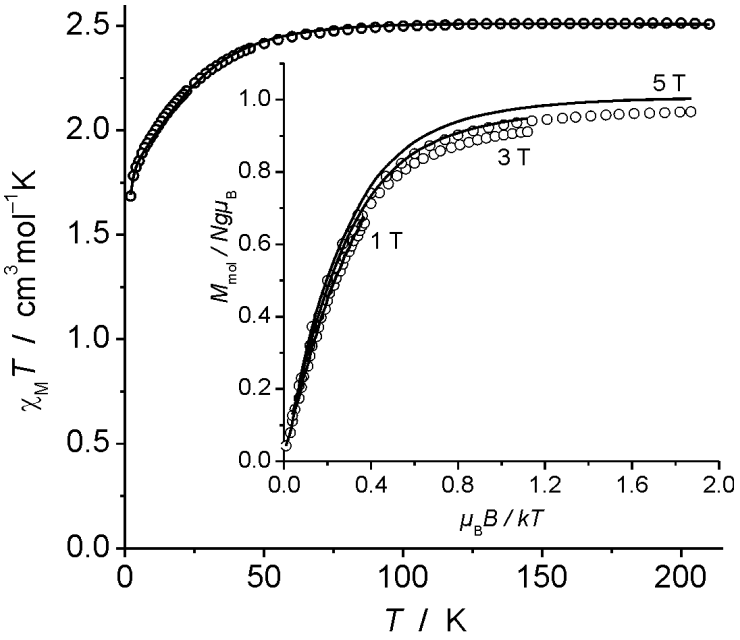


**Figure S12**. $\chi_M T$ versus $T$ plot for **1**. Insert: variable temperature–variable field (VTVH) magnetization measurements as $M_{mol}$ versus $\mu_B B/kT$.

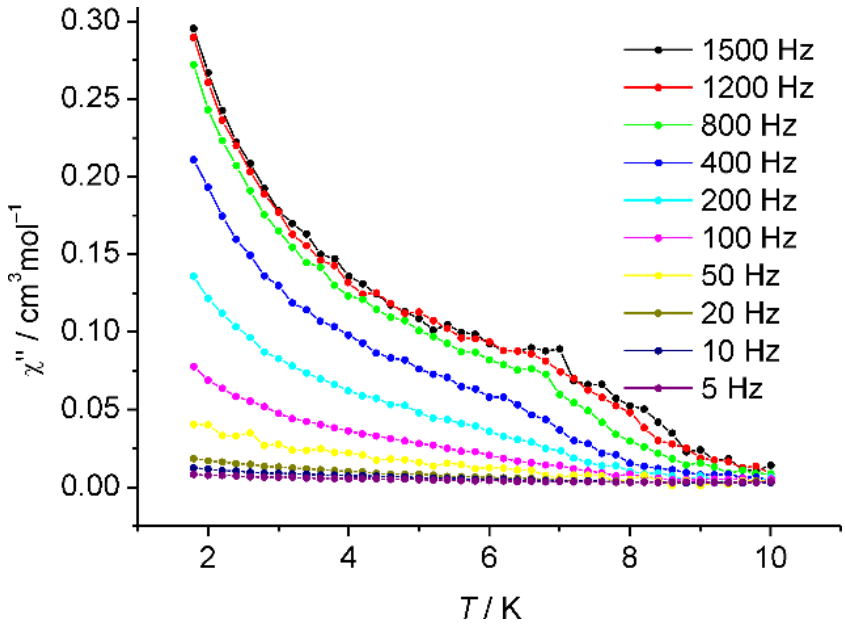


**Figure S13**. Temperature dependence of $\chi$'' at various frequencies in the absence of a DC field.

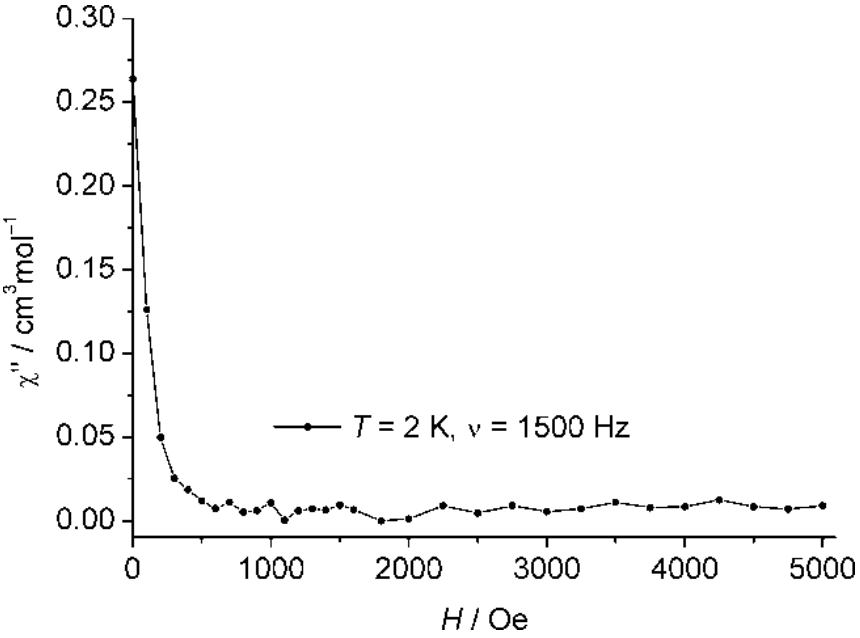


**Figure S14**. Field dependence of $\chi$'' at 2 K using 1500 Hz AC frequency.

Temperature dependence of the obtained relaxation times $\tau$ is shown in Figure S14 (calculated as $\tau = 1/2\pi\nu$, with $T$ values being the peak temperatures of $\chi$'' at given frequency, see Figure 2 of the manuscript).

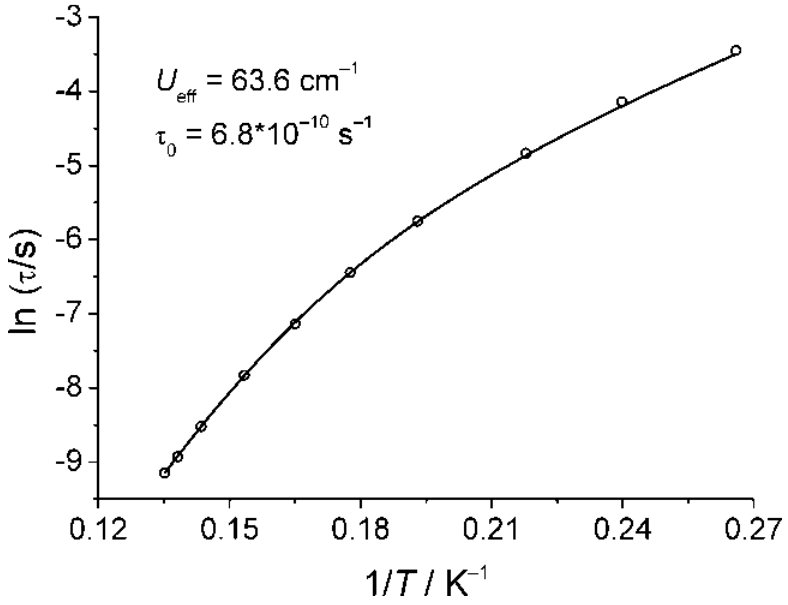


**Figure S15**. Arrhenius plot of the temperature dependence of $\tau$ for **1** with an applied dc field of $H_{DC}$ = 1000 Oe.

The obtained points are clearly deviating from a linear Arrhenius law, hence additional relaxation processes have to be considered. In general, the temperature dependence of the

relaxation times can be described according to (eq. 2) with three different types of relaxation: direct, Raman and Orbach processes.[13]

$$\tau^{-1} = AH^4T + BT^n + \tau_0^{-1}\exp\left(-U_{eff}/k_BT\right) \quad \text{(eq. 2)}$$

To avoid the overparametrization, only the Raman term ($BT^n$) was added to the linear Orbach dependence (in coordinates $\ln\tau$ vs. $1/T$, Arrhenius law), while the $AH^4T$ term was fixed to zero. The obtained best fit parameters are $B$ = 4.4·10$^{-3}$ K$^{-6.7}$·s$^{-1}$, $n$ = 6.7, $U_{\text{eff}}$ = 63.6 cm$^{-1}$ and $\tau$ = 6.8·10$^{-10}$ s.

## 4 Mössbauer spectroscopy

Mössbauer spectra were recorded with a $^{57}$Co source in a Rh matrix using an alternating constant acceleration *Wissel* Mössbauer spectrometer operated in the transmission mode and equipped with a *Janis* closed-cycle helium cryostat. Isomer shifts are given relative to iron metal at ambient temperature. Simulation of the experimental data was performed with the programs *Mfit* and *MX* (E. Bill, Max-Planck Institute for Chemical Energy Conversion, Mülheim/Ruhr, Germany). The zero-field spectrum at 80 K has been fitted as an asymmetric Lorentzian doublet, and the magnetically split Mössbauer spectrum at 7 K was simulated by diagonalization of the spin Hamiltonian for the electronic ground state of Fe(I) with $S$ = 3/2. Hyperfine interaction for the $^{57}$Fe nuclei was calculated by using the usual nuclear Hamiltonian.[14]

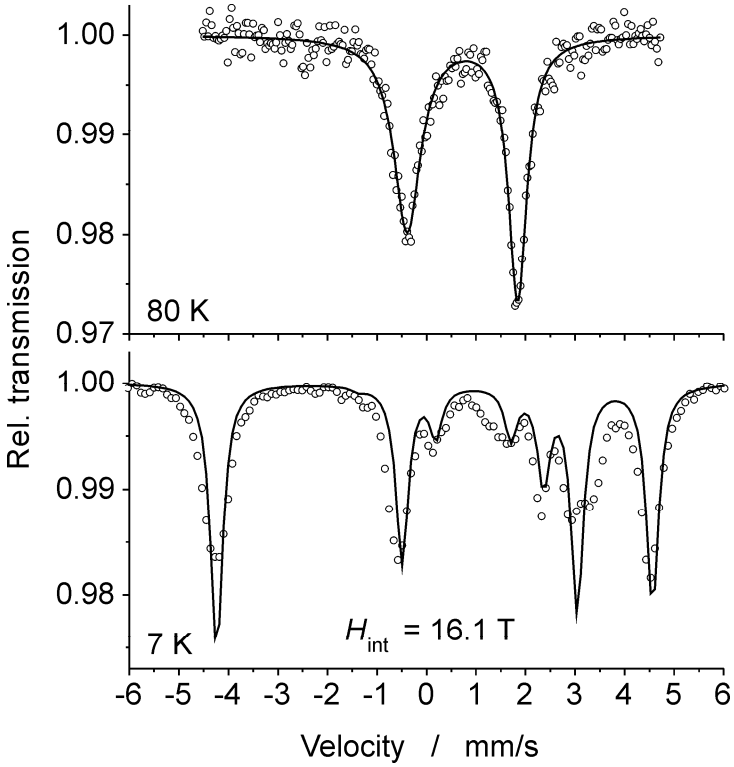


**Figure S16**. Mössbauer spectra for **1** at 80 K (top) and 7 K (bottom) in the solid state without external magnetic field. The solid lines represent fits with a Lorentzian doublet (80 K, best fit parameters are $\delta$ = 0.72 mm/s and $\Delta E_Q$ = 2.23 mm/s) or a spin Hamiltonian simulation for $S$ = 3/2 (7 K, best fit parameters are $g_x = g_y$ = 2.20, $g_z$ = 2.50, $D$ = –33 cm$^{-1}$, $\delta$ = 0.72 mm/s, $\Delta E_Q$ = 2.40 mm/s and $H_{int.}$ = 16.1 T).

## 5 EPR spectroscopy

The experimental X-band EPR spectrum of **1** was recorded on a Bruker EMX spectrometer (Bruker BioSpin Rheinstetten) equipped with a He temperature control cryostat system (Oxford Instruments). EPR spectroscopic measurements revealed that the Fe(I) complex **1** is nearly EPR silent, as can be expected for an S = 3/2 system with a *negative* zero field splitting parameter D. The $\Delta m_s = 3$ transition within the magnetic ground state $|m_s\rangle = |\pm 3/2\rangle$ Kramers doublet is formally forbidden, and hence associated with a very weak signal intensity. As such, EPR measurements at 30 K using a microwave power of ~1 mW showed only the signals of a minor S = ½ impurity in the sample (< 0.1% of the total Fe concentration according to spin integration measurements, see Figure S14). Only when recording the X-band EPR spectra with a high microwave power (200 mW) and at a lower temperature (8 K), a derivative signal corresponding to the main S = 3/2 species became visible (Figure S15). Simulation of the EPR signal was performed using the EPR simulation program W95EPR developed by Prof. Dr. Frank Neese (Brute Force mode) in order to estimate the magnitude of the real $g_z$-value from the measured $g_{eff}$ value (Figure S15).

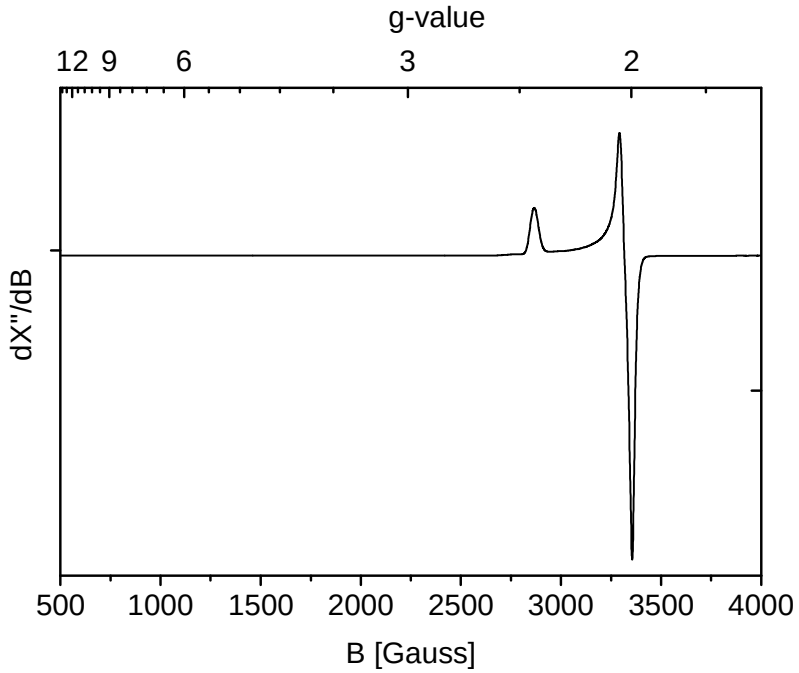


**Figure S17**. X-band EPR spectrum of a minor S = ½ impurity present in the sample of **1** recorded in frozen toluene at 30 K. This signal represents < 0.1% of the total Fe concentration according to spin integration measurements (double integral of this signal relative to that of a [Co(TPP)] reference sample with known concentration). Experimental parameters: Frequency 9.384169 GHz, microwave power = 0.632 mW, modulation amplitude = 6 G.

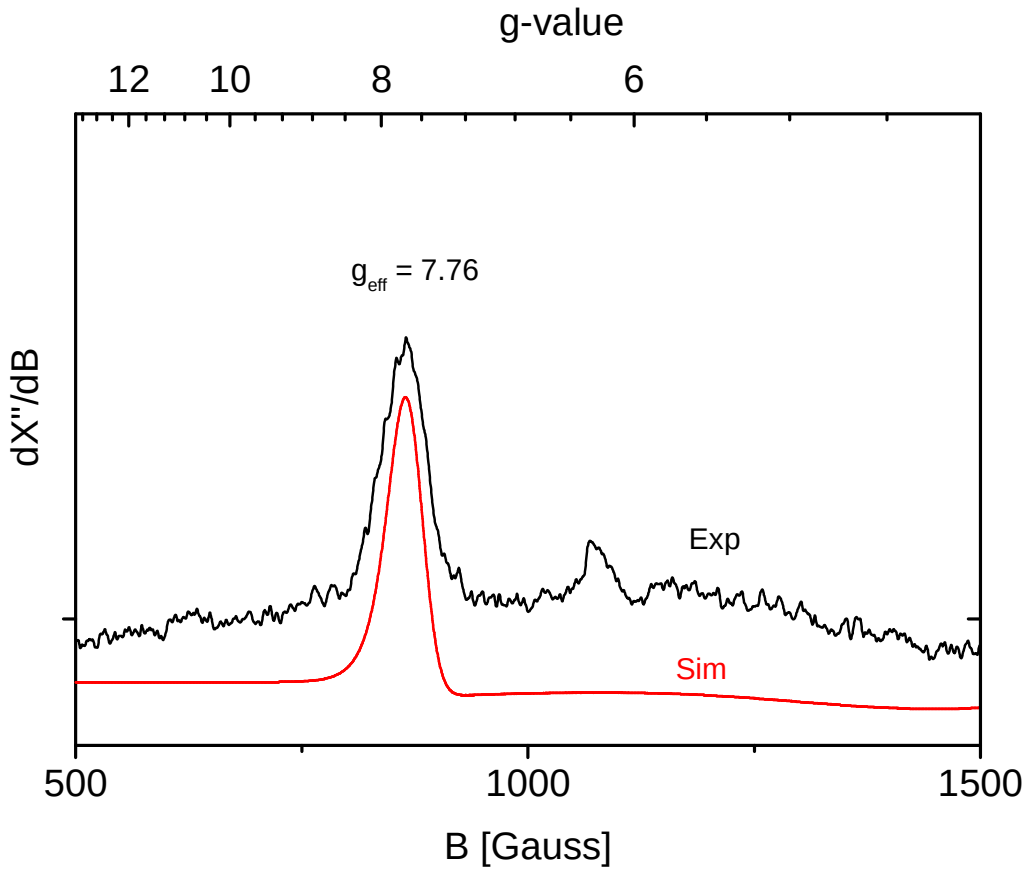


**Figure S18**. Eperimental and simulated X-band EPR spectrum of Fe(I) compound **1** recorded in frozen toluene at 8 K and measured with a high microwave power of 200 mW, showing the weak, forbidden $\Delta m_s = 3$ transition within the $|m_s\rangle = |\pm 3/2\rangle$ Kramers doublet of the S = 3/2 (D < 0, E/D ~ 0) species. Frequency 9.384207 GHz, modulation amplitude = 6 G. The simulation was obtained with the following parameters: S = 3/2, $g_x = g_y = 2.18$, $g_z = 2.55$, $W_x = W_y = 1500$, $W_z = 200$, D = –33.4 $cm^{-1}$, E/D = 0.001, T = 8 K (only $g_{z,eff}$ is resolved).

## 6 Quantum chemical calculations

### Computational details

All calculations were carried out with the ORCA suite of electronic structure programs.[15,16] In order to compute magnetic parameters, we have relied on state-average complete active space self-consistent field (SA-CASSCF) method[17] with all electron basis sets as mentioned above. For the $d^7$ ions, the active space is comprised of CAS(7,5) (three active electrons in the five active orbitals). Here, we have computed ten quartets and (unless otherwise specified) all the forty doublet states in the configuration interaction (CI) procedure. The molecular orbitals have been optimized in an average way for all the states belonging to the given multiplicity. To capture, the effect of the dynamic correlations, we have performed second order N-electron valence (NEVPT2) method[18] on top of the converged CASSCF wave function. The resolution of identity (RI) approximation[19] has been used with the corresponding auxiliary basis sets in order to speed up the calculations. The spin-orbit effects along with the Zeeman interactions are incorporated by quasi-degenerate perturbation theory (QDPT) approach, where the spin-orbit mean field (SOMF) operator[20] lead to a mixing of different multiplicities ($\Delta S = 0, \pm 1$). Magnetic parameters have been computed using effective Hamiltonian theory developed by J. P. Marieu and N. Guitery[21] as implemented in the ORCA program package. Matrix elements of dipole transitions have been computed following ref. [22].

### Interpretation and comparison with experiment

Two-coordinate linear first row metal complexes with σ- and π-donor ligands possess a simple 3d-orbital scheme with non-bonding $d_{xy}$, $d_{x2-y2}$, π-antibonding $d_{xz}$,$d_{yz}$ and σ-antibonding $d_{z2}$. Energy expressions for the 3d-orbitals approximated by the angular overlap model are given by:

$$d_{z2} : 2e_{\sigma} - 4e_{sd} \qquad (1)$$

$$d_{xz}, d_{yz} : 2e_{\pi} \qquad (2)$$

$$d_{x2-y2}, d_{xy} : 0 \qquad (3)$$

with $e_{\sigma}$ and $e_{\pi}$ -energy destabilization induced by a single ligand. The parameter $e_{sd}$ in eq.1 accounts for the mixing (hybridization) of the $3d_{z2}$ and 4s orbitals in linear complexes which lowers (highers) the energy of $d_{z2}(4s)$ by $4e_{sd}$. Depending on the strength of the metal-

ligand bond, $d_{z2}$ may be shifted below $d_{xz}, d_{yz}$ and may (in limiting cases $2e_\sigma - 4e_{sd} \leq 0$) become non-bonding or even fall down below $d_{x2-y2}, d_{xy}$.

For a complex with the energy level scheme of Figure 2 perturbation theory yields the following expressions for spin-Hamiltonian (eq.4) parameters *D* and *E* and for the g-tensor: $g_z$, $g_x$ and $g_y$:

$$H_{SH} = D\left[S_z^2 - S(S+1)/3\right] + E(S_x^2 - S_y^2) + \mu_B(H_x g_x S_x + H_y g_y S_y + H_z g_z S_z) \qquad (4)$$

$$D = -\frac{4}{9}\frac{\zeta^2}{\Delta E}; E = 0 \qquad (5)$$

$$g_z = 2 + \frac{4}{3}\frac{\zeta}{\Delta E}; g_x = g_y = 2.00 \qquad (6)$$

Using $\zeta$ and $\Delta E$ values from the NEVPT2 calculation (348 and 942, respectively), a rough estimate of *D* and $g_z$ using eqs. (5) and (6) yields $D = -59.2$ cm$^{-1}$ and $g_z = 2.51$, and the following values for the g-tensor of the ground state Kramers doublet ($M_s = \pm 3/2$):

$$\begin{aligned} g_z(M_s = \pm 3/2) &= 3g_z = 7.53 \\ g_{x,y}(M_s = \pm 3/2) &\approx 0 \end{aligned} \qquad (7)$$

These simple considerations readily explain i) the large and negative ($D = -33.4$ cm$^{-1}$) extracted from the magnetic data, and ii) the value of $g_{eff} = 7.76$ from X-band EPR. However, as shown by the NEVPT2 results, the low symmetry of the complex allows orbital mixing, which results in off-axial anisotropy and modifies these parameters, leading to $D = -42.02$ cm$^{-1}$, $E = -0.50$ cm$^{-1}$, and $g_z = 8.362$, $g_{x,y}(M_s = 3/2) = 0.075$. The small yet non-negligible non-zero values of *E* is responsible for the observation of the intra-Kramers doublet in the X-band EPR. The underlying reason is mixing of the $M_s = \pm 3/2$ ground term spin with the $M_s = \pm 1/2$ excited state term.

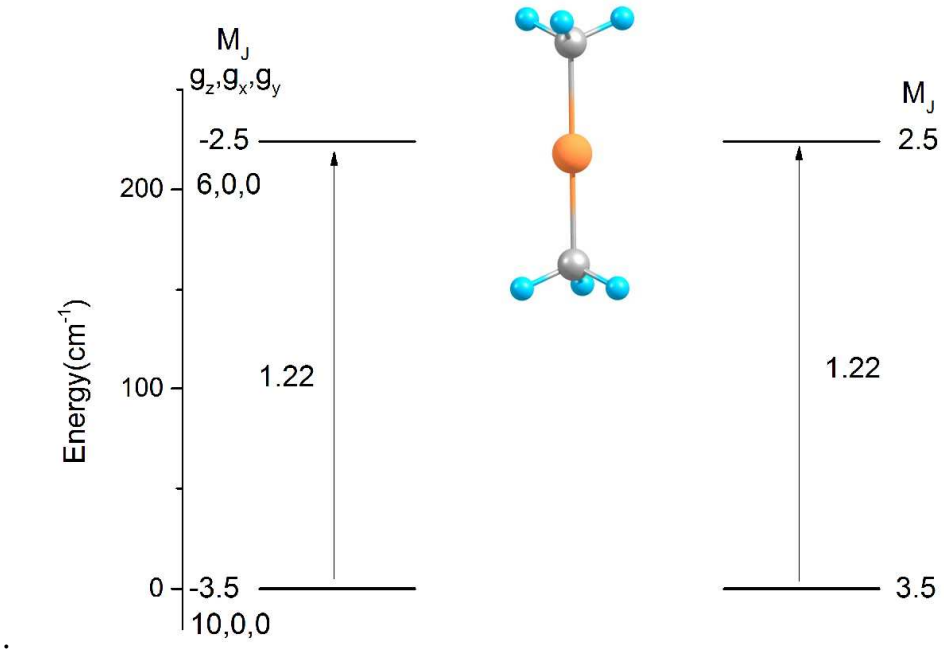


**Figure S19**. Effective $M_J$ and ground and excited state main g-tensor components for a linear $[Fe(CH_3)_2]^-$ model complex with ideal $D_{3d}$ symmetry

**Ab-initio ligand field results and their analysis using ascending symmetry series decomposition of the ligand field matrix**

Ab-initio ligand field theory (now being implemented in the ORCA 4.0) yields the parameters of the ligand field: the Racah parameters of interelectronic repulsion (B, C), the spin-orbit coupling (ζ) and the 5x5 ligand field matrix $V_{LF}$ resulting from both CASSCF and CASSCF/NEVPT2 calculation. Values of the parameters extracted from the CASSCF/NEVPT2 calculation are:

B=722 $cm^{-1}$, C=3122 $cm^{-1}$, ζ=348 $cm^{-1}$,

and

| $V_{LF}(cm^{-1})$ | $d_{xy}$ | $d_{yz}$ | $d_{z2}$ | $d_{xz}$ | $d_{x2-y2}$ |
|---|---|---|---|---|---|
| $d_{xy}$ | 148 | -102 | -114 | -1423 | 11 |
| $d_{yz}$ | -102 | 1218 | 1618 | -164 | 1280 |
| $d_{z2}$ | -114 | 1618 | 750 | 46 | 714 |
| $d_{xz}$ | -1423 | -164 | 46 | 2740 | -42 |
| $d_{x2-y2}$ | 11 | 1280 | 714 | -42 | -148 |

Here we should note that the form of the ligand field matrix will depend on the choice of the laboratory coordinate system. This choice is of course not unique. In our calculation we have chosen such an orientation of the coordinate system which approximately [23] matches the canonical axes of the ZFS tensor and the g-matrix of the Spin-Hamiltonian of eq.4. The rather low-symmetry ($C_1$) of complex **1** is reflected in $V_{LF}$ by the rather large off-diagonal elements between the $d_{xz}$-$d_{xy}$(-1423 $cm^{-1}$) and $d_{yz}$-$d_{x2-y2}$(1280 $cm^{-1}$) pairs of orbitals and by the very large splitting (1522 $cm^{-1}$) reflected by the diagonal elements of $d_{xz}$ and $d_{yz}$ orbitals reflected by the diagonal matrix elements corresponding to these orbitals, 2740 $cm^{-1}$ and 1218 $cm^{-1}$, respectively. The splitting between the $d_{xz}$ and $d_{yz}$ orbitals is due to the planar N-heterocyclic carbene (NHC) ligand with out-of-plane π-orbitals available for metal 3d-ligand overlap. Being engaged in strong C-N within the NHC plane, π orbitals within the NHC plane for metal 3d-ligand overlap are missing –a very large π-anisotropy of the Fe-C(NHC) bond results. The large off-diagonal elements between the $d_{xz}$-$d_{xy}$ and $d_{yz}$-$d_{x2-y2}$ orbitals results from the tilting of the $CP^{Ar}$ ligand with respect to the Fe-C(NHC) bond direction (the angle $Cp^{Ar}$(centr)-Fe1-C1 = 162.1$^o$ deviates considerably from 180$^o$. The effects of the geometry of complex **1** and the intrinsic structures of the $CP^{Ar}$ and NHC ligands on the ligand field may be further quantified

using ascending symmetry series decomposition of the ligand field matrix of 1 eq.8 into $C_1$, $C_{2v}$ and $C_{\infty v}$ increments.[24,25]

$$V_{LF} = V_{LF}(C_1) + V_{LF}(C_{2v}) + V_{LF}(C_{\infty v}) \qquad (8)$$

In this representation of $V_{LF,}$ $V_{LF}(C_1)$ (eq.9) has been approximated by the off-diagonal elements of $V_{LF}$, $V_{LF}(C_{2v})$ (eq.10) by the $C_{2v}$ splitting of $d_{xz}$,$d_{yz}$ and $d_{x2\text{-}y2}$,$d_{xy}$, while $V_{LF}(C_{\infty v})$ (eq.10) by their averaged energies as follows:

$$V_{LF}(C_1) = \begin{bmatrix} 0 & -102 & -114 & -1423 & 11 \\ -102 & 0 & 1618 & -164 & 1280 \\ -114 & 1618 & 0 & 46 & 714 \\ -1423 & -164 & 46 & 0 & -42 \\ 11 & 1280 & 714 & -42 & 0 \end{bmatrix} \qquad (9)$$

$$V_{LF}(C_{2v}) = \begin{bmatrix} 148 & 0 & 0 & 0 & 0 \\ 0 & -761 & 0 & 0 & 0 \\ 0 & 0 & 750 & 0 & 0 \\ 0 & 0 & 0 & 761 & 0 \\ 0 & 0 & 0 & 0 & -148 \end{bmatrix} \qquad (10)$$

$$V_{LF}(C_{\infty v}) = \begin{bmatrix} 0 & 0 & 0 & 0 & 0 \\ 0 & 1979 & 0 & 0 & 0 \\ 0 & 0 & 750 & 0 & 0 \\ 0 & 0 & 0 & 1979 & 0 \\ 0 & 0 & 0 & 0 & 0 \end{bmatrix} \qquad (11)$$

The effect of the perturbations described by $V_{LF}(C_{2v})$ and $V_{LF}(C_1)$ on $V_{LF}(C_{\infty v})$ has been illustrated pictorially in Figure S20. From this plot we can infer, that the $C_{\infty v}$ component of the ligand field yields a rather sizable contribution to the entire ($C_1$) ligand field splitting (as much as roughly ½ of the total splitting!). The changes with decrease of symmetry from $C_{\infty v}$ to $C_{2v}$ illustrate and quantify: i) the large $d_{xz}$ and $d_{yz}$ splitting arising from the π-anisotropy of the NHC ligand (vide supra) and ii) the first order splitting of the $d_{x2\text{-}y2}$, $d_{xy}$ orbital pair. The letter splitting results from the σ/π mixing between the $d_{z2}$ and $d_{x2\text{-}y2}$ orbitals, both being of the same $a_1$ symmetry in the $C_{2v}$. This mixing leads to a decrease of the energy of the $3d_{x2\text{-}y2}$ MO with

respect to dxy ($a_2$). Finally, the large off-diagonal elements $d_{xz}$-$d_{xy}$(-1423 $cm^{-1}$) and $d_{yz}$-$d_{x2-y2}$(1280 $cm^{-1}$) are stemming from the bending of the structure leading to mixing of the two sets of orbitals (see above). This bending increases the energies of both 3d MOs $d_{xz}$ and $d_{yz}$ leading to the computed 3d molecular energy pattern of **1**, particularly the small energy separation between the two topmost orbitals. The right and the left parts of the orbital diagram of Figure S20 have been used to construct Figure 3a and the corresponding part of Figure 3b.

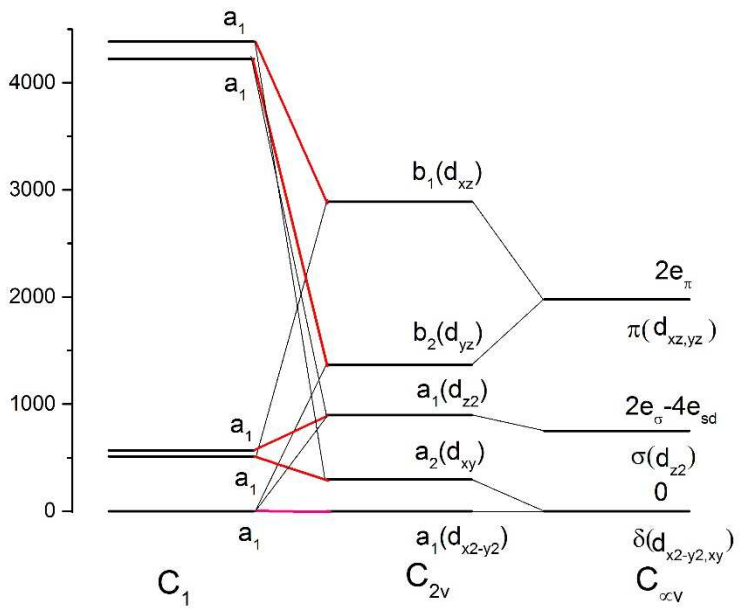


**Figure S20:** 3d-MOs (NEVPT2) of **1** in ascending order of symmetries starting from $C_1$ as computed for **1**, to $C_{2v}$ to $C_{\infty v}$, the latter referring to the component of the ligand corresponding to a cylindrically averaged electron density within the complex with π-isotropic 3d-metal-ligand interactions. The correlation of the 3d-MOs for are shown using connecting lines; for $C_1$ leading contributions to each 3d MO are shown by thick lines highlighted in red.

## References


[1] U. Chakraborty, M. Modl, B. Mühldorf, M. Bodensteiner, S. Demeshko, N. J. C. van Velzen, M. Scheer, S. Harder, R. Wolf, *Inorg. Chem.* **2016**, *55*, 3065.

[2] N. Kuhn, T. Kratz, *Synthesis* **1993**, 561.

[3] N. Blaquiere, S. Diallo-Garcia, S. I. Gorelsky, D. A. Black, K. Fagnou, *J. Am. Chem. Soc.* **2008**, *130*, 14034–14035.

[4] a) D. R. Anton, R. H. Crabtree, Organometallics **1983**, 2, 855; b) G. Franck, M. Brill, G. Helmchen, J. Org. Chem. **2012**, 89, 5.

[5] a) J. A. Widegren, R. G. Finke, *J. Mol. Catal. A* **2003**, *198*, 317; b) R. H. Crabtree, *Chem. Rev.* **2012**, *112*, 1536; c) J. F. Sonnenberg, R. H. Morris, *Catal. Sci. Technol.* **2014**, *4*, 3426.

[6] J. R. Vance, A. Schäfer, A. P. M. Robertson, K. Lee, J. Turner, G. R. Whittell, I. Manners, *J. Am. Chem. Soc.* **2014**, *136*, 3048.

[7] CrysAlisPro Software System, Agilent Technologies UK Ltd, Yarnton, Oxford, UK, **2013**.

[8] O. V. Dolomanov, L. J. Bourhis, R. J. Gildea, J. A. K. Howard, H. Puschmann, *J. Appl. Cryst.*, 2009, **42**, 339.

[9] G. M. Sheldrick, *Acta Cryst.*, 2008, **A64**, 112.

[10] M. Reiners, D. Baabe, K. Harms, M. Maekawa, C. G. Daniliuc, M. Freytag, P. G. Jones, M. D. Walter, *Inorg. Chem. Front.* **2015, *3*, 250**.

[11] Y. Ohki, T. Hatanaka, K. Tatsumi, *J. Am. Chem. Soc.* **2008**, *130*, 17174.

[12] O. Kahn *Molecular Magnetism*, VCH Publishers Inc., New York, **1993**.

[13] R. L. Carlin, *Magnetochemistry*, Springer-Verlag, Berlin - Heidelberg **1986**.

[14] P. Gütlich, E. Bill, A. X. Trautwein, *Mössbauer Spectroscopy and Transition Metal Chemistry*, Springer, Heidelberg, **2011.**

[15] F. Neese, Comput. Mol. Sci., 2012, 2 73-78.

[16] ORCA - an ab initio, DFT and semiempirical SCF-MO package - Version 4.0, Design and Scientific Directorship: F. Neese, Technical Directorship: F. Wennmohs, Max-Planck-Institute for Chemical Energy Conversion Stiftstr. 34-36, 45470 Mülheim a. d. Ruhr, Germany, tccec@mpi-mail.mpg.de, With contributions from: D. Aravena, M. Atanasov, U. Becker, D. Bykov, D. Datta, A. Kumar Dutta, D. Ganyushin, Y. Guo, A. Hansen, L. Huntington, R. Izsak, C. Kollmar, S. Kossmann, M. Krupicka, D. Lenk, D. G. Liakos, D. Manganas, D. A. Pantazis, T. Petrenko, P. Pinski, C. Reimann, M. Retegan, C. Riplinger, T. Risthaus, M. Roemelt, M. Saitow, B. Sandhöfer, I. Schapiro, K. Sivalingam, G. Stoychev, B. Wezisla; and contributions

from our collaborators: M. Kallay, S. Grimme, E. Valeev, G. Chan, J. Pittner; additional contributions to the manual from: G. Bistoni, W. Schneider.

[17] a) P.-Å. Malmqvist, B.O. Roos, *Chem. Phys. Lett.* **1989**, *155*, 189-194; b) K. Wolinski, P. Pulay, *J. Chem. Phys.* **1989**, *90*, 3647-3659; c) K. Andersson, P. Å. Malmqvist, B. O. Roos, A. J. Sadlej, K. Wolinski, *J. Phys. Chem.* **1990**, *94*, 5483-5488; d) K. Andersson, P. Å. Malmqvist, B.O. Roos, J. Chem. Phys. **1992**, *96*, 1218; e) B. O. Roos, P.-A. Malmqvist, *Phys. Chem. Chem. Phys.* **2004**, *6*, 2919-2927. f) B. Roos, M. Fülscher, P.-Å. Malmqvist, M. Merchán, L. Serrano-Andrés, S. Langhoff (ed.), *Quantum Mechanical Electronic Structure Calculations with Chemical Accuracy*, Springer Netherlands, **1995**, pp. 357-438.

[18] a) C. Angeli, R. Cimiraglia, S. Evangelisti, T. Leininger, J.-P. Malrieu, *J. Chem. Phys.* **2001**, *114*, 10252-10264; b) C. Angeli, R. Cimiraglia, J.-P. Malrieu, *Chem. Phys. Lett.* **2001**, *350*, 297-305; c) C. Angeli, R. Cimiraglia, J.-P. Malrieu, *J. Chem. Phys.* **2002**, *117*, 9138-9153; d) C. Angeli, B. Bories, A. Cavallini, R. Cimiraglia, *J. Chem. Phys.* **2006**, *124*, 054108.

[19] F. Neese, *J. Comput. Chem.* **2003**, *24*, 1740.

[20] a) B. A. Hess, C. M. Marian, U. Wahlgren, O. Gropen, *Chem. Phys. Lett.* **1996**, *251*, 365; b) F. Neese, *J. Chem. Phys.* **2005**, *122*, 034107.

[21] a) J. P. Malrieu, P. Durand, J. P. Daudey, *J. Phys. A: Math. Gen.* **1985**, *18*, 809-826; b) R. Maurice, C. de Graaf, N. Guihéry, *J. Chem. Phys.* **2010**, *133*, 084307; c) R. Maurice, R. Bastardis, C. de Graaf, N. Suaud, T. Mallah, N. Guihéry, *J. Chem. Theory Comput.* **2009**, *5*, 2977 ; d) R. Maurice, N. Guihéry, C. de Graaf, *J. Chem. Theory Comput.* **2010**, *6*, 55; e) R. Maurice, A. M. Pradipto, N. Guihéry, R. Broer, C. de Graaf, *J. Chem. Theory Comput.* **2010**, *6*, 3092.

[22] a) L. Ungur, L. F. Chibotaru, *Phys. Chem. Chem. Phys.* DOI:10.1039/cicp22689d; b) L. Ungur, M. Thewissen, J.-P. Costes, W. Wernsdorfer, L. F. Chibotaru, *Inorg. Chem.* **2013**, *52*, 6328-6337; explicitly we used the following equation for the magnetic dipole transition matrix element $\mu_{if}$ linking two magnetic states: initial, $|i\rangle$ and *final* $|f\rangle$: $\mu_{if} = (|\langle i|\mu_x|f\rangle| + |\langle i|\mu_y|f\rangle| + |\langle i|\mu_z|f\rangle|)/3$ with $\mu_x$, $\mu_y$ and $\mu_z$ – the components of the magnetic moment operator.

[23] In a strict sense, the canonical axes of the ZFS-tensor(x',y',z') and the g-matrix (x",y",z") are not co-linear. The mismatch between the two sets of axes normally does not exceed 2-3°.

[24] The procedure has been elaborated and applied to the electronic structure of the $3d^q$, $4d^2$ and $5d^2$ ions by M. Brorson and C. E. Schaffer, *Inorg. Chem.* **1988**, *27*, 2522-2530. Operators representing one- or two-electron ligand field effect are normally chosen in the form of bari-centered matrices. The matrices $V_{LF}(C_1), V_{LF}(C_{2v})$ and $V_{LF}(C_{\infty v})$ have been set-up taking the average energy of $d_{x2-y2}$ and $d_{xy}$ as reference.

[25] In some sense, this decomposition of the ligand field of eq.8 is the energetic ligand field analogue of the countinuous symmetry measure concept put forward by D. Anvir et al. The latter along with the implemented algorithm (the program SHAPE) allows to deduce the departure of a low-symmetry complex from a higher symmetric one with the same number of ligands, see: a) J. Cirera, E. Ruiz, S. Alvarez, *Organometallics* **2005**, *24*, 1556−1562; b) S. Alvarez, P. Alemany, D. Casanova, J. Cirera, M. Llunell, D. Avnir, *Coord. Chem. Rev.* **2005**, *249*, 1693−1708; c) S. Alvarez, *Chem. Rev.* **2015**, *115*, 13447−13483 and original references given therein.